Electronic Supplementary Material (ESI) for Chemical Science.

Supplementary information

Identifying the Active Sites and Intermediates on Copper Surfaces for Electrochemical Nitrate Reduction to Ammonia

Yohan Kim,[a, †] Jinyoung Ko,[b ,c, †] Minyoung Shim,[a] Jiwon Park,[a] Hyun-hang Shin,[d] Zee Hwan Kim,[d] Yousung Jung,[b, c, *] and Hye Ryung Byon [a,*]

[a] Department of Chemistry, Korea Advanced Institute of Science and Technology (KAIST), 291, Daehak-ro, Yuseong-gu, Daejeon 34141, Republic of Korea

[b] Department of Chemical and Biomolecular Engineering, Korea Advanced Institute of Science and Technology (KAIST), 291 Daehak-ro, Yuseong-gu, Daejeon 34141, Republic of Korea

[c] School of Chemical and Biological Engineering, Seoul National University, Seoul 08826, Republic of Korea

[d] Department of Chemistry, Seoul National University, Seoul 08826, Republic of Korea

[†] Contributed equally to this work

*E-mail: hrbyon@kaist.ac.kr, yousung.jung@snu.ac.kr

Experimental details

Preparation of Cu electrodes

Cu foils were purchased from Alfa Aesar (0.025mm thick, Puratronic®, 99.999% (metals basis)) and cut in 2.5 cm × 1 cm area. This Cu foil was washed sequentially with acetone (CH_3COCH_3, 99.5%, Samchun), isopropanol (IPA, $(CH_3)_2CHOH$, 99.9%, Samchun), and de-ionized water (DI water, 18.2 MΩ) for 5 min each in bath sonication. The washed Cu foil, w-Cu, was dried by an air blower and kept in a vacuum. To prepare acid-etched Cu, *a*-Cu, *w*-Cu was soaked in 10 mL of glacial acetic acid (CH_3COOH, ≥ 99.7%, Sigma Aldrich) for 5 min.[1] The etched Cu was thoroughly rinsed with DI water and dried in a vacuum. To form electropolished Cu (*e*-Cu), *w*-Cu was set as the working electrode in an electrochemical cell and connected with another Cu as the counter electrode. With phosphoric acid (H_3PO_4, ≥85 wt. % in H_2O, Sigma Aldrich) electrolyte solution, 2 V was applied for 5 min.[2, 3] Afterwards, electropolished *w*-Cu was washed with DI water and dried by an air blower. All Cu foils were prepared just before electrochemical measurements and surface analyses to mitigate air oxidation of the Cu surfaces.

Electrochemical measurements

All electrochemical measurements were conducted using a gas-tightened H-cell comprised of the working- and counter-electrode chambers (**Figure S3**). As-prepared Cu foils were employed as the working electrode, and Graphite rod (6.15 mm diameter × 102 mm lengths, 99.9995% (metal basis), Alfa Aesar) and Hg/HgO (1 M NaOH) were used as the counter and reference electrode respectively. Nafion 212 was used as the cation-exchange membrane between working- and counter-electrode chambers in the H-cell, where H^+ was exchanged with K^+. This cation exchange was attained by soaking as-received Nafion 212 in 30 wt% H_2O_2 (Sigma Aldrich) for 12 h, neat H_2SO_4 (99.999%, Sigma Aldrich) for 12 h, followed by 1 M KOH (Semiconductor grade, 99.99%, Sigma Aldrich) solution overnight.

A 1 M KOH aqueous solution was the electrolyte solution. The electrolyte solutions were Ar-bubbled (99.999% purity) at least 30 min before the cell assembly, and this Ar-saturated condition was maintained during electrochemical measurements by continuously introducing Ar gas to the gas-tightened cell. Applying potential was corrected by *iR*-compensation with an 85% level before tests and was calibrated to the reversible hydrogen electrode (RHE) with consideration in the residual 15% *iR*-compensation after tests. The potential calibration equation is as follows (Eq. S1),

$$E \text{ (vs. RHE)} = E \text{ (vs. Hg/HgO)} + 0.140 + 0.0592 \times \text{pH (14)} - 0.15 \times i \times R \qquad \text{(Eq. S1)}$$

where E (vs. Hg/HgO) is the measured potential, i is the current, and R is the uncompensated resistance.

For nitrate reduction reaction (NO_3RR), 50 mM KNO_3 (99.99%, Sigma Aldrich) was added to a 1 M KOH electrolyte solution. To identify each cathodic wave signal, 50 mM $NaNO_2$ (99.999%, Sigma Aldrich) or 50 mM $NH_2OH{\cdot}HCl$ (ACS reagent, ≥99.0%, Sigma Aldrich) was added instead of KNO_3.

Electric double layer capacitances (EDLCs) were measured by cyclic voltammetry in − 0.44 ~ − 0.46 V vs. Hg/HgO potential range and 10 ~ 50 mV s^{-1} scan rates. At each scan rate, charging current density (J_{charging}) was calculated by averaging the current density of the anodic scan (J_{anodic}) and cathodic scan (J_{cathodic}) (Eq. S2).

$$J_{\text{charging}} = 0.5 \times (J_{\text{anodic}} - J_{\text{cathodic}}) \qquad \text{(Eq. S2)}$$

Electrochemical impedance spectroscopy (EIS) was measured in a frequency range of 10^6 ~ 10^{-1} Hz with 10 mV voltage amplitude.

Characterizations

Cu foil surfaces were analyzed using a scanning electron microscope (SEM, Hitachi, SU5000) and atomic force microscope (AFM, Agilent 5500 SPM). Root-mean-square (RMS) surface roughness was estimated by Gwyddion software of AFM, an environmental scanning electron microscopy (ESEM, Quattro S, FEI) with electron backscatter diffraction (EBSD) mode. X-ray photoelectron spectroscopy (XPS, Thermo VG Scientific, K-alpha) and linked Auger spectroscopy were used to detect Cu valence states. All spectra were calibrated with C1s sp^3 hybridization to 284.8 eV. For the deconvolution of Cu LMM Auger spectra, commercial CuO (99.99%, Sigma Aldrich) and Cu_2O (99.99%, Sigma Aldrich) were used as the standard material.[4, 5] The metallic Cu^0 spectrum was obtained from *w*-Cu which was Ar^+ sputtered for 30 sec. The transmission electron microscopy (TEM, Talos F200X, Thermo Fisher) analysis, coupled with focused ion beam (FIB, Helios G4, FEI) sample fabrication, was accomplished to measure the thickness of the oxide layer on *w*-Cu. Pt of C was deposited before the FIB milling process to protect the sample surface. The cross-sectional sample thickness was controlled near 70 nm. The FIB sample was prepared at the KAIST Analysis Center for Research Advancement (KARA). For isotope tests, ^{1}H NMR (500 MHz, Bruker AVANCE NEO, Bruker) was utilized to detect NH_4^+. The NH_4^+ solution was prepared by standard NH_4Cl (99.99%, Sigma Aldrich), $^{15}NH_4Cl$ (≥98 atom% ^{15}N, Sigma Aldrich), or electro-synthesized from $K^{14}NO_3$ or $K^{15}NO_3$ (98 atom % ^{15}N, Sigma Aldrich).

Quantitative product analysis – ammonia (NH_3)

The quantity of ammonia was analyzed using the UV-Vis colorimetric method, with Nessler reagent (Sigma Aldrich) as the coloring reagent.[6-8] Because UV-Vis absorptions of the Nessler reagent relied on solution pH, we prepared calibration curves for the working-electrode chamber and the acid-trap container separately because ammonia was collected from both containers.

For the calibration curve of the working-electrode chamber, standard ammonium solutions were prepared with 0.32, 0.64, 1.00, 2.01, 3.01, 4.01, and 5.02 mg L^{-1} concentrations in 0.1 M KOH solution. For the acid-trap container, 1.00, 2.01, 3.01, 4.01, and 5.02 mg L^{-1} of standard solutions were prepared in 5 mM H_2SO_4 solution.

For the NO_3RR product analysis, the analyte (electrolyte solution) in the working-electrode chamber was collected and diluted 50 times using 0.1 M KOH solution. The analyte in the acid-trap container was collected and diluted 10 times using 5 mM H_2SO_4.

The above standard solutions or analytes 5 mL were injected into a 0.5 mL of 0.2 M potassium sodium tartrate tetrahydrate ($KNaC_4H_4O_6{\cdot}4H_2O$, 99%, Sigma Aldrich) aqueous solution. Then, 0.5 mL of Nessler reagent was added, and the solution was shaken thoroughly. After waiting for color development for 20 min, UV-Vis absorption at 420 nm was measured using Lamda 265 spectrometry (Felkin Almer). These works were repeated three times for each, and the resulting independent measurements were averaged with the standard deviation.

Faradaic efficiency (FE), partial current density (J_{NH_3}), and yield were estimated by following equations (Eqs. S4-6), where C is the concentration, V is the electrolyte volume, F is the Faradaic constant, $J_{averaged}$ is the averaged current density during 1 h chronoamperometry tests at the given potential, and A is the electrode surface area.

$$\mathrm{FE\ (NH_3,\ \%)} = \frac{C_{NH_3}\left(mol\,L^{-1}\right) \times V\,(L) \times F\,(C\,mol^{-1}) \times 8}{total\ electron\ pass\ (C)} \times 100 \qquad \text{(Eq. S4)}$$

$$J_{\mathrm{partial}}\ (\mathrm{NH_3,\ mA\ cm^{-2}}) = \mathrm{FE_{NH_3}}\ (\%) \times J_{\mathrm{averaged}}\ (\mathrm{mA\ cm^{-2}}) \qquad \text{(Eq. S5)}$$

$$\mathrm{Yield\ (NH_3,\ \mu mol\ cm^{-2}\ h^{-1})} = \frac{C_{NH_3}\left(\mu mol\,L^{-1}\right) \times V\,(L)}{A\,(cm^2) \times 1\,h} \qquad \text{(Eq. S6)}$$

Quantitative product analysis – nitrite (NO_2^-)

The nitrite was detected by Griess reaction[6-8] and qualified using the UV-Vis colorimetric method. Standard nitrite solutions were prepared at 0.10, 0.20, 0.30, 0.40, 0.50, and 1.00 mg L^{-1} concentration in DI water for the calibration curve. The coloring reagent of the Griess test was prepared by mixing 2 g of sulfanilamide (≥99.0%, TCI), 0.1 g of N-(1-Naphthyl) ethylenediamine (>98%, Sigma Aldrich), 5 mL of 85 wt% H_3PO_4 (Sigma Aldrich), and 25 mL of DI water. Afterward, 5 mL of the standard solution and 0.1 mL of the coloring solution were mixed. After 20 min waiting, UV-Vis absorption was measured at 540 nm. Three independent measurements were repeated, and absorbances were averaged with the standard deviation. A similar method also detected the analyte after 1 h of chronoamperometry tests. The analyte solution was only collected from the working electrode chamber and diluted 800 times using DI water.

FE, $J_{NO_2^-}$, and yield were estimated by following equations (Eqs. S7-9).

$$\mathrm{FE\ (NO_2^-,\ \%)} = \frac{C_{NO_2^-}\left(mol\,L^{-1}\right) \times V\,(L) \times F\,(C\,mol^{-1}) \times 2}{total\ electron\ pass\ (C)} \times 100 \qquad \text{(Eq. S7)}$$

$$J_{\mathrm{partial}}\ (\mathrm{NO_2^-,\ mA\ cm^{-2}}) = \mathrm{F}^{E}{}_{NO_2^-}\ (\%) \times J_{\mathrm{averaged}}\ (\mathrm{mA\ cm^{-2}}) \qquad \text{(Eq. S8)}$$

$$\text{Yield } (NO_2^-, \mu\text{mol cm}^{-2}\text{ h}^{-1}) = \frac{C_{NO_2^-}\ (\mu mol\ L^{-1}) \times V\ (L)}{A\ (cm^2) \times 1\ h} \qquad \text{(Eq. S9)}$$

Au@SiO_2 nanoparticle preparation for enhanced Raman spectroscopy

For *operando* electrochemical shell-isolated nanoparticle enhanced Raman spectroscopy (SHINERS) analysis, SiO_2 shell-isolated Au nanoparticle (Au@SiO_2) was synthesized, referred to in the previous report.[9] First, the Au seed particle was synthesized. A 20 mL of 0.01 wt% chloroauric acid (99.99%, Alfa Aesar) was injected in a round-bottom flask and heated to boil at 100 °C. After adding 0.2 mL of 1 wt% sodium citrate (99.0%, Sigma Aldrich) and 30 min holding, the solution was cooled to room temperature. Afterward, 2 mL of Au seed particle (~40 nm) was added to a new round-bottom flask with 26.5 mL of DI water. The solution was blended with 0.45 mL of 1 wt% sodium citrate and stirred for 3 min, followed by adding 0.45 mL of chloroauric acid (1 wt%) and stirred for 8 min. Finally, 0.7 mL of 10 mM hydroxylamine hydrochloride ($NH_2OH{\cdot}HCl$, Sigma Aldrich) was dropped wisely for 5 min under stirring, and the solution was stirred 1 h further. Through this process, the Au nanoparticle size became enlarged to 150 nm. The solution (a total of 15 mL) was diluted to 30 mL using DI water, and 0.5 mL of 0.5 mM (3-Aminopropyl)triethoxysilane (APTES, Sigma-Aldrich) was injected, followed by an additional 20 min stirring. To coat the Au nanoparticles with the SiO_2 shell, 2.8 mL of 0.54 wt% sodium silicate solution (27% SiO_2, Sigma-Aldrich) was added to the prepared solution and stirred for 3 min. Then, the solution was heated to 90 °C in a water bath, stirred for 1 h, and rapidly cooled down using an ice bath. The solution was washed and centrifuged with DI water 5 times to obtain Au@SiO_2 nanoparticles. (Relative centrifugal force as 598 g for 10 min) Synthesized nanoparticles were characterized by XPS, SEM, and TEM (FEI Company, Tecnai F20).

A 20 μL of Au@SiO_2 nanoparticle solution was diluted using 20 μL of IPA and mixed with 2 μL of 0.25 wt% Nafion solution (DE520, Ion power). 5 μL of this solution was drop cast on the Cu electrode, and electrodes were dried in a vacuum desiccator at least 15 min before *operando* electrochemical Raman measurements.

Operando electrochemical shell-isolated nanoparticle enhanced Raman spectroscopy (SHINERS) measurements

As shown previously,[9-11] thin SiO_2 layers in SHIN effectively quench any electrochemical reaction on the Au surface while maintaining the strongly confined electromagnetic field for sensitive surface-enhanced Raman scattering (SERS) detection of surface species on Cu surfaces. As SHIN, Au@SiO_2 nanoparticles were prepared with 150 nm-diameter Au core and 5 nm-thickness SiO_2 shell (see the above and **Figure S16**) and drop-cast onto Cu electrodes after being mixed with Nafion binder that was used for stable attachment. These Au@SiO_2 nanoparticles amplify the Raman signal by plasmonic (**Figure S17**).[9-11]

Raman microscope (Andor Shamrock SR-750, Oxford Instruments) with a 633 nm excitation laser source was used for *operando* electrochemical SHINERS analysis. A light was focused onto the sample through a water-immersion objective lens (LUMPLFLN40XW, Olympus, numerical aperture: 0.8) covered with PFA film (perfluoroalkoxy, 0.05 mm thickness, AS ONE), and the same objective lens was used to collect the SERS radiation. A droplet of DI water was placed between the objective lens and the PFA film to adjust the refractive index of the electrolyte solution. *Operando* electrochemical Raman cell (K008, ida) was used, where leak-free Ag/AgCl (3.4 M KCl) and Pt wire were employed as the reference and counter electrode, where negligible Pt contamination was expected for a short reaction time. All the electrochemical measurements were conducted using an electrochemical workstation (SP-150, Biologic). The cathodic reaction was conducted to the Au@SiO_2 drop-cast Cu foil (1.5 cm × 2.5 cm area) as the working electrode by holding a constant potential for 5 min and measuring Raman spectroscopy for 30 s exposure at the same potential. This process was repeated from 0.0 V to –0.5 V with a –0.1 V gap.

Computational details

Raman peak prediction

The theoretical Raman peak positions were obtained from the density functional theory (DFT) calculation, which employs the Gaussian 09 package.[12] We utilized a 6-311G++ (d, p) basis set for free molecules without metals. For the Cu-molecule complexes, we utilized the combined basis sets of LanL2DZ (Cu atom) and 6-311G++ (d, p) (molecular part), using the multi-layered

ONIOM (Our own N-layered Integrated molecular Orbital and molecular Mechanics)[13, 14] methods.

Free energy calculation

All DFT calculations were performed using the Vienna Ab initio Simulation Package (VASP) coupled with the Hubbard U correction.[15-17] The projector augmented wave (PAW) method was used, and the Perdew-Burke-Ernzerhof (PBE) functional was applied for all the structural optimizations.[18, 19] Plane waves with an energy cutoff of 400 eV were applied, and U values (employed as U-J) of 3.6 were applied for Cu_2O and 7.14 for CuO for delocalization issues of standard DFT.[20-22] In addition, we employed the dispersion-corrected DFT-D method for long-range interactions like van der Waals interactions.[23] In each structural model, a vacuum layer of 15 Å was set to avoid the influence of interaction between the top and bottom slab. Also, each structural model consists of four atomic layers, two of which are fixed at the bottom to simulate the bulk phase of the model. The Brillouin zone was sampled by the Monkhorst-Pack scheme, and the k points of 3×3×1, 3×3×1, and 3×2×1 were applied for the Cu, Cu_2O, and CuO surfaces, respectively.[24] The convergence criteria for the energy and interatomic forces are set 10^{-5} eV and 0.03 eV/Å, respectively. Since the reduction process proceeded in an aqueous environment and involved *H transfer, the solvent effect was considered for all adsorbents with implicit solvation models.[25] A dipole correction was considered along the vertical direction to minimize inaccuracies in the total energy because of simulated slab interaction.[26] Minimum energy paths and saddle points for all structural models were found using the climbing image nudged elastic band (CI-NEB) method.[27]

For each step, the reaction free energy (Δ^{G_R}) is calculated by

$$\Delta^{G_R} = \Delta^{E} + \Delta^{ZPE} - T\Delta^{S} \qquad \text{(Eq. S10)}$$

where ΔE is the total energy difference between reactants and products, ΔS is the change in entropy for each reaction, T is the temperature (298.15 K), ΔZPE and is the zero-point energy correction to the reaction free energy. In this way, the reaction-free energy of intermediates can be calculated. When a reaction proceeds in a solution at pH apart from 0, the free energy that H^+ takes part in is corrected by

$$\Delta G_H = -k_B T \ln 10 * \mathrm{pH} \qquad \text{(Eq. S11)}$$

where k_B is Boltzmann’s constant and T is the temperature.[28]

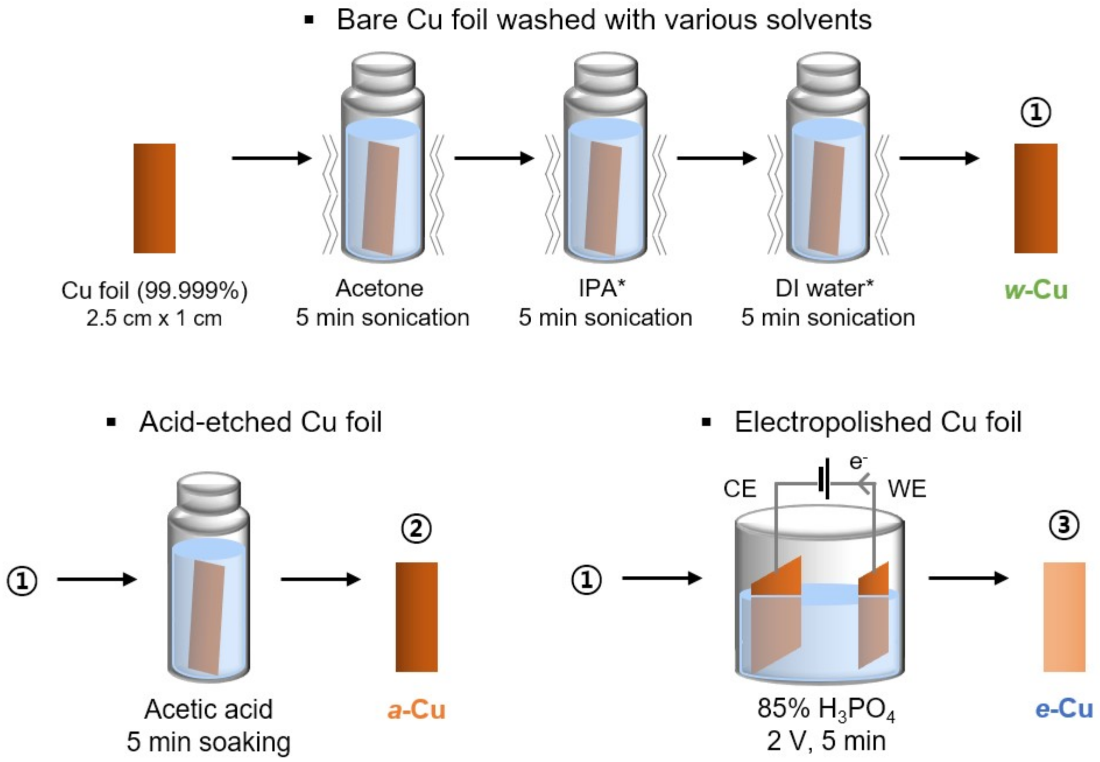

Scheme S1. Fabricating methods of electrodes. The *w*-Cu was prepared by sequential bath sonication of as-received Cu foil in acetone, isopropanol (IPA), and DI water. The *a*-Cu was prepared by soaking *w*-Cu in glacial acetic acid for 5 min. The *e*-Cu was formed by electrochemical oxidation of *w*-Cu in 85 wt% H_3PO_4 by applying 2 V from another Cu foil as the counter electrode.

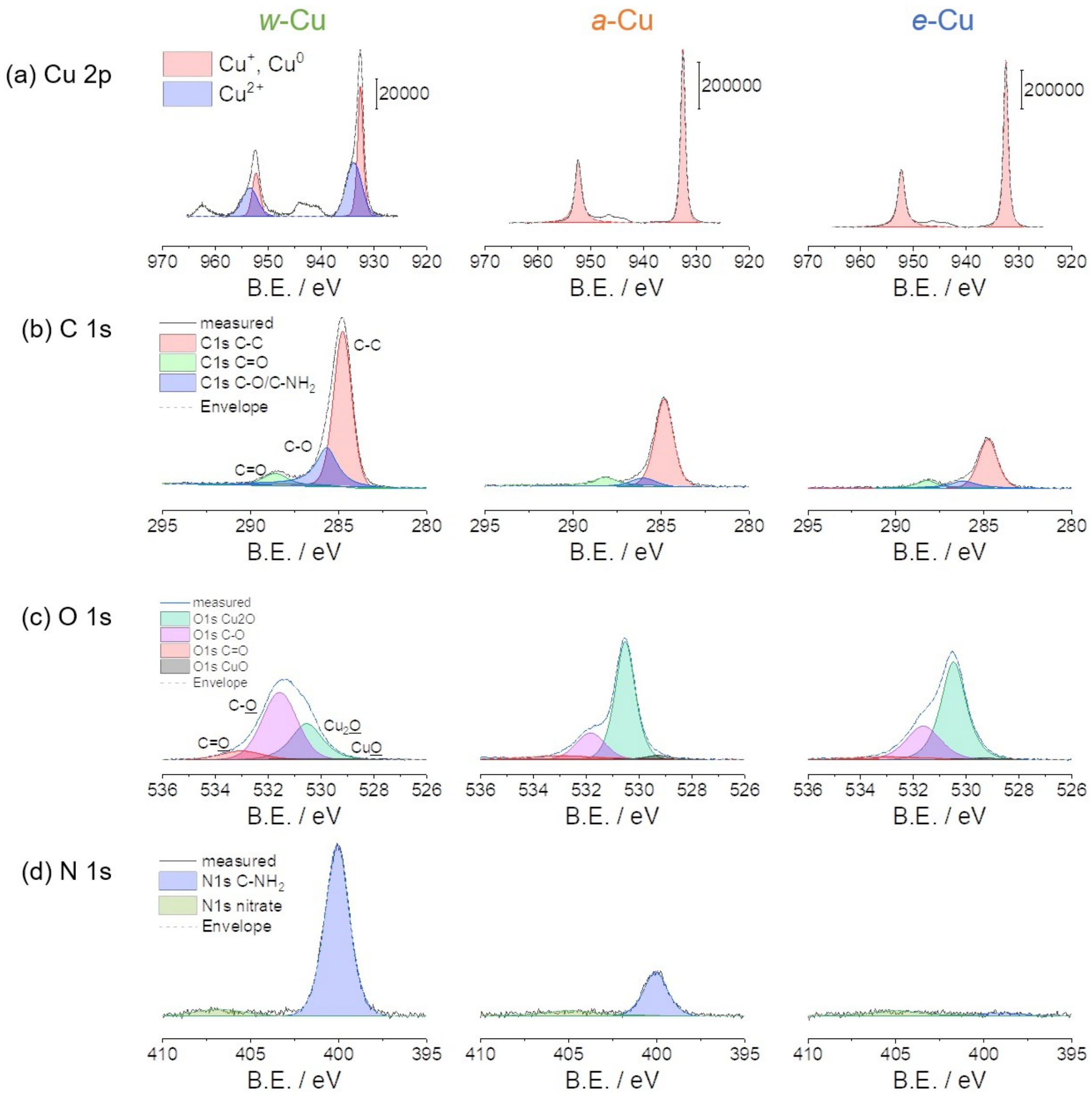

Figure S1. XPS analysis of as-prepared *w*-Cu, *a*-Cu, and *e*-Cu (from left to right). XPS spectra are in (a) Cu 2p, (b) C 1s, (c) O 1s, and (d) N 1s binding energy (BE) regions.

Assigned signals are as follows. Cu 2p: $Cu^{+/0}$ (932.5, 952.3 eV), Cu^{2+} (933.8, 953.4 eV), [29-31] C 1s: $\underline{C}$-C (284.8 eV), $\underline{C}$-O (285.7 eV), $\underline{C}$=O (288.6 eV),[30] O 1s: Cu$\underline{O}$ (529.3 eV), $Cu_2\underline{O}$ (530.5 eV), C-$\underline{O}$ (513.6 eV), C=$\underline{O}$ (532.9 eV),[29, 31] and N 1s: C-$\underline{N}H_2$ (400.1 eV), and $\underline{N}O_3^-$ (406.8 eV). The N 1s signals were referred to the 2012 NIST XPS database.[32]

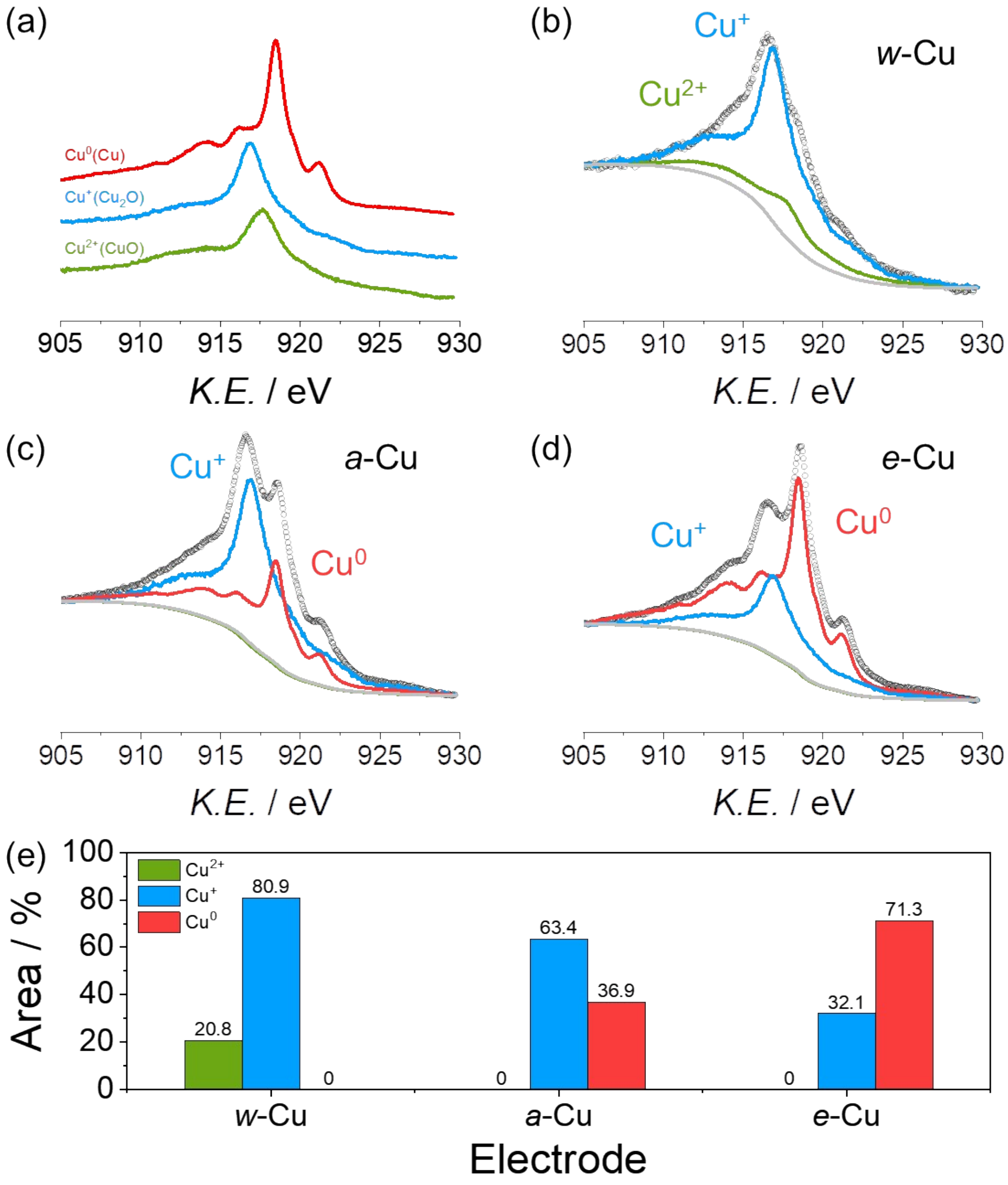

Figure S2. Quantitative analysis of Cu LMM spectra by the linear combination fitting of the standard material spectra. (a) CuO (Cu^{2+}), Cu_2O (Cu^+), and metallic Cu (Cu^0) standard spectra. (b-d) Deconvoluted sample spectra of as-prepared (b) *w*-Cu, (c) *a*-Cu, and (d) *e*-Cu. (e) Comparative area percentage of Cu^{2+}, Cu^+, and Cu^0 for as-prepared samples.

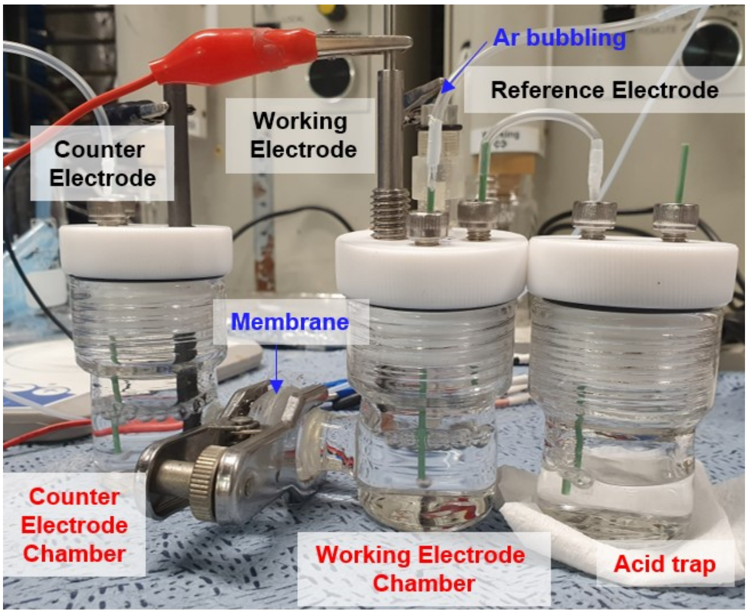

Figure S3. Digital photo of gas-tightened H-cell, comprised of working-electrode and counter-electrode chamber, linked with acid-trap container. The Cu electrode, graphite rod, and Hg/HgO (1 M NaOH) are working, counter, and reference electrodes. An Ar-purged 1 M KOH aqueous solution was electrolyte, where 50 mM KNO_3 was added for NO_3RR tests. A membrane was Nafion 212, where H^+ was exchanged with K^+. The acid trap container included 5 mM H_2SO_4 aqueous solution with Ar bubbling and served as capturing vaporized NH_3. For quantitative NH_3 analysis, evolving gas was collected from the working electrode chamber and the acid trap.

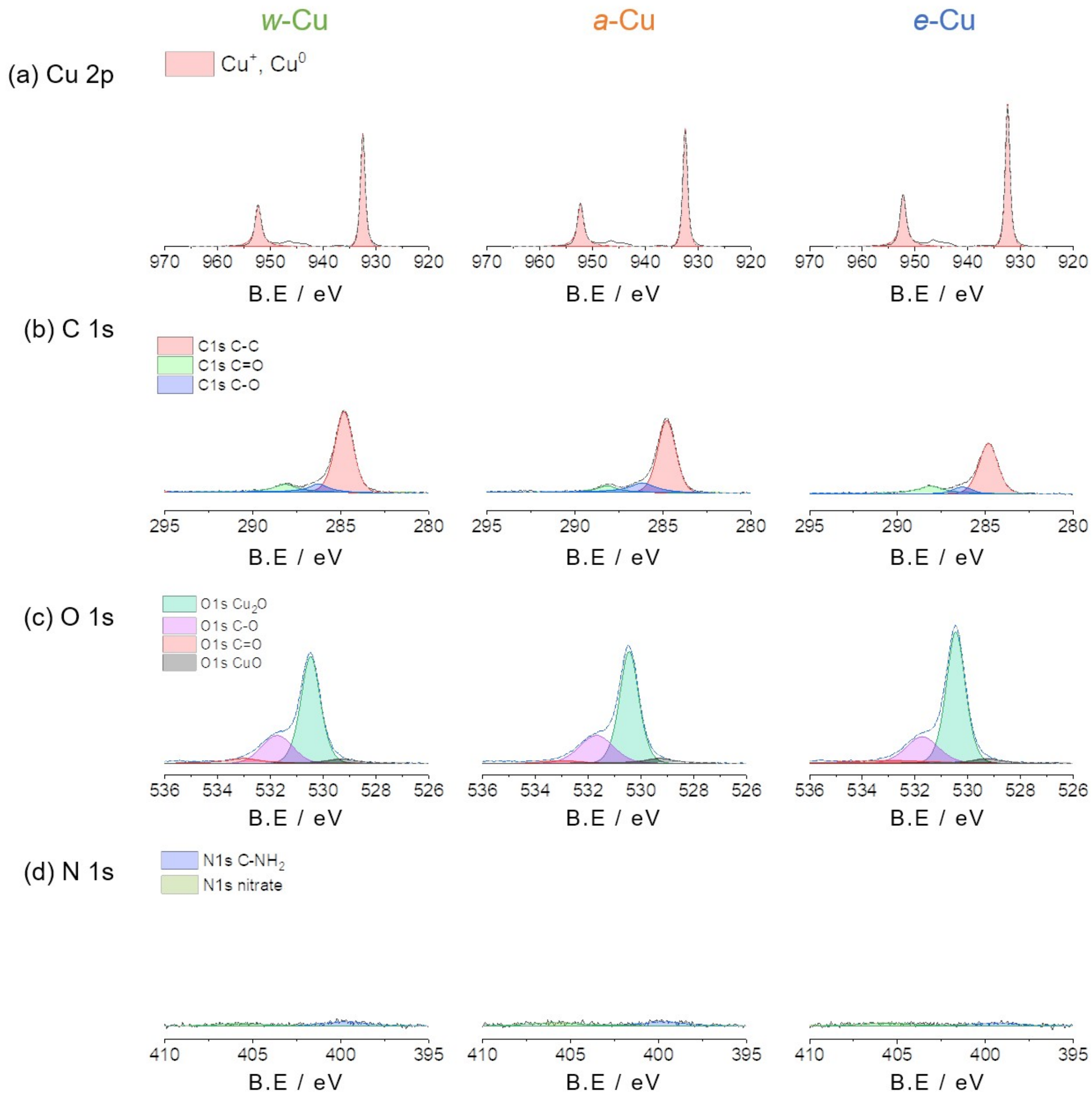

Figure S4. XPS analysis of *w*-Cu, *a*-Cu, and *e*-Cu (from left to right) after 10 min of soaking in an Ar-saturated 1 M KOH solution with 50 mM KNO_3 electrolyte. XPS spectra are in (a) Cu 2p, (b) C 1s, (c) O 1s, and (d) N 1s binding energy (BE) regions.

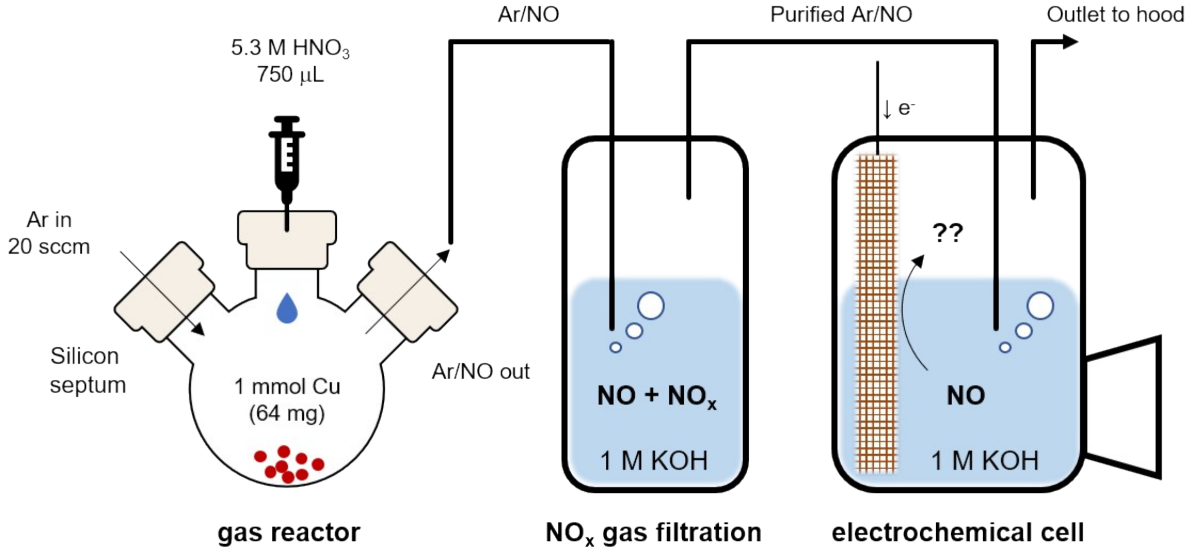

$8HNO_3 + 3Cu \rightarrow 3Cu(NO_3)_2 + 4H_2O + \mathbf{2NO}$

Scheme S2. The schematic illustration of an electrochemical cell linked with an in-situ NO gas generation reactor was modified from the previous report.[33] NO/NO_x gas evolves from the gas-reactor cell, where neat nitric acid and copper powder are reacted. NO/NO_x gas flows to the NO_x gas filtration cell through the Ar stream (20 sccm), where a 1 M KOH solution selectively filters NO gas from NO_x ($x \geq 2$) impurity. The NO gas finally introduces the electrochemical cell.

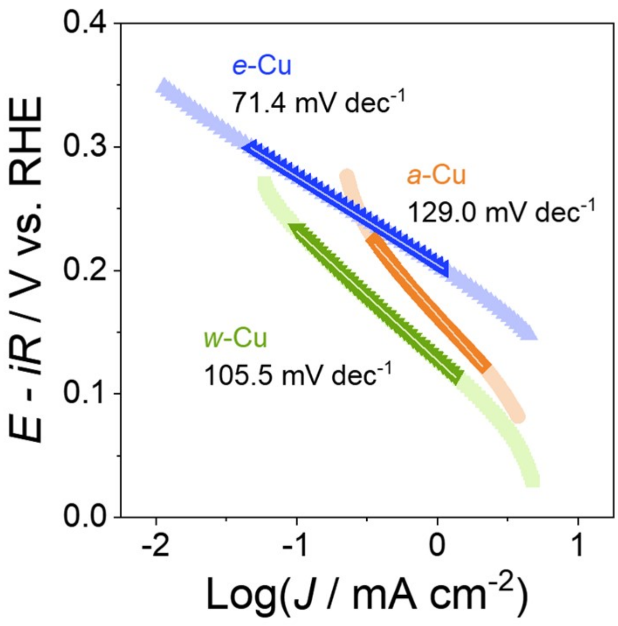

Figure S5. Tafel slopes of 50 mM NO_3^- reduction close to the onset potential of each electrode.

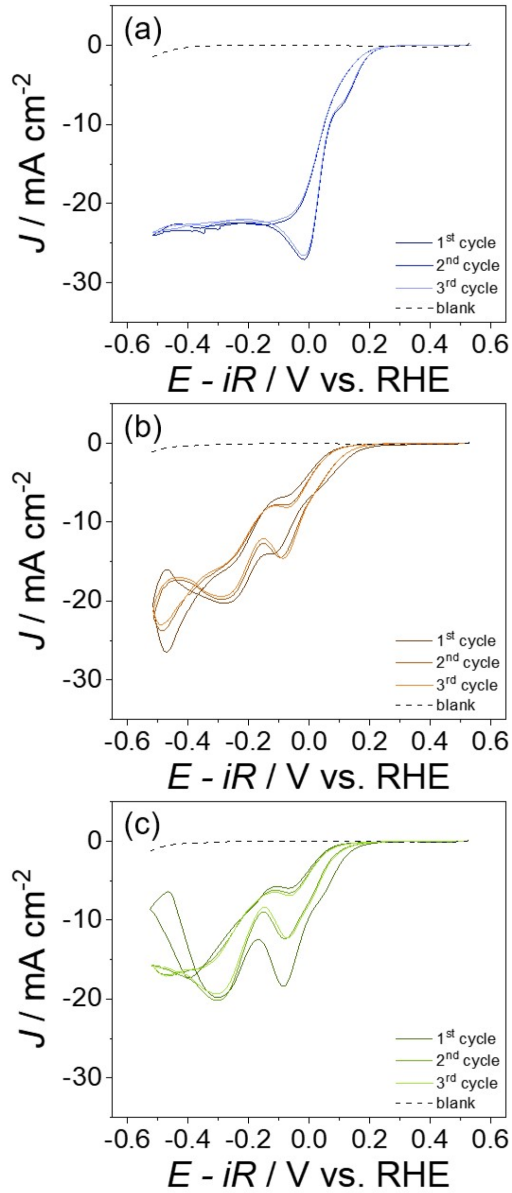

Figure S6. Cyclic voltammogram (CV) of 50 mM NO_3^- reduction during 3 cycles for (a) *e*-Cu, (b) *a*-Cu, and (c) *w*-Cu electrode. The blank (dashed lines) indicated a KNO_3-free electrolyte solution.

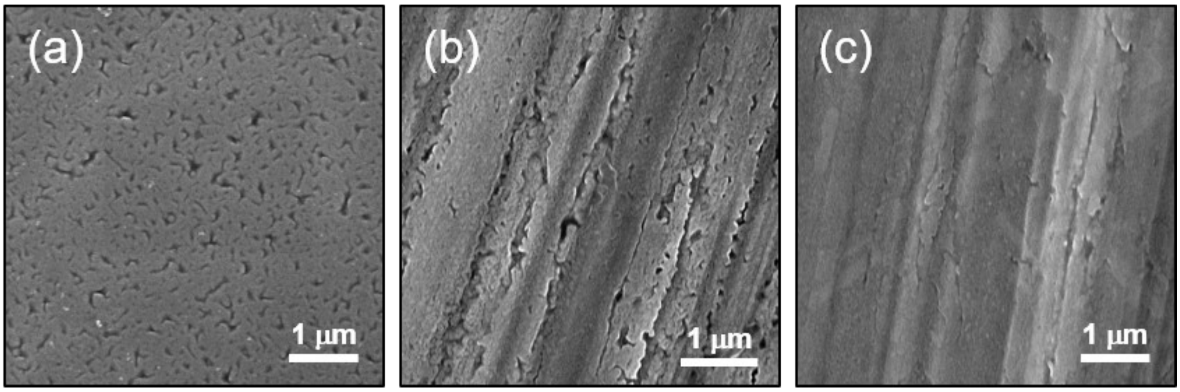

Figure S7. SEM image of Cu surfaces after 3 cycles of CV in 50 mM KNO_3 and 1 M KOH electrolyte solution (**Figure S6**). The electrodes are (a) *e*-Cu, (b) *a*-Cu, and (c) *w*-Cu.

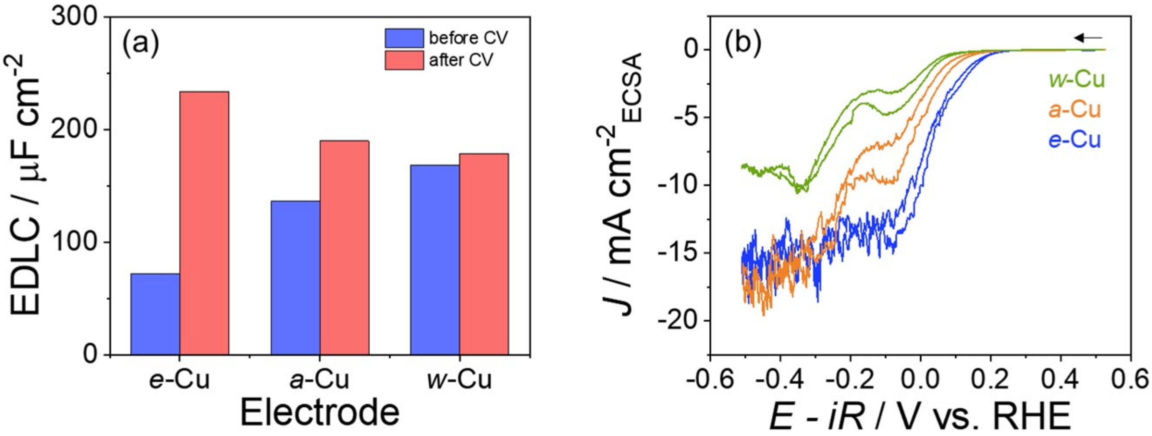

Figure S8. Electrical double layer capacitance (EDLC) measurements for *w*-Cu, *a*-Cu, and *e*-Cu electrodes before and after 4 cycles of CV in 50 mM KNO_3 and 1 M KOH electrolyte solution with Ar bubbling at 20 sccm. (a) Estimated EDLC before and after CV cycles. (b) Electrochemical surface area (ECSA)-normalized current density (*J*) for the fourth cycled CVs. Detailed calculations of ECSA are shown in **Table S3**.

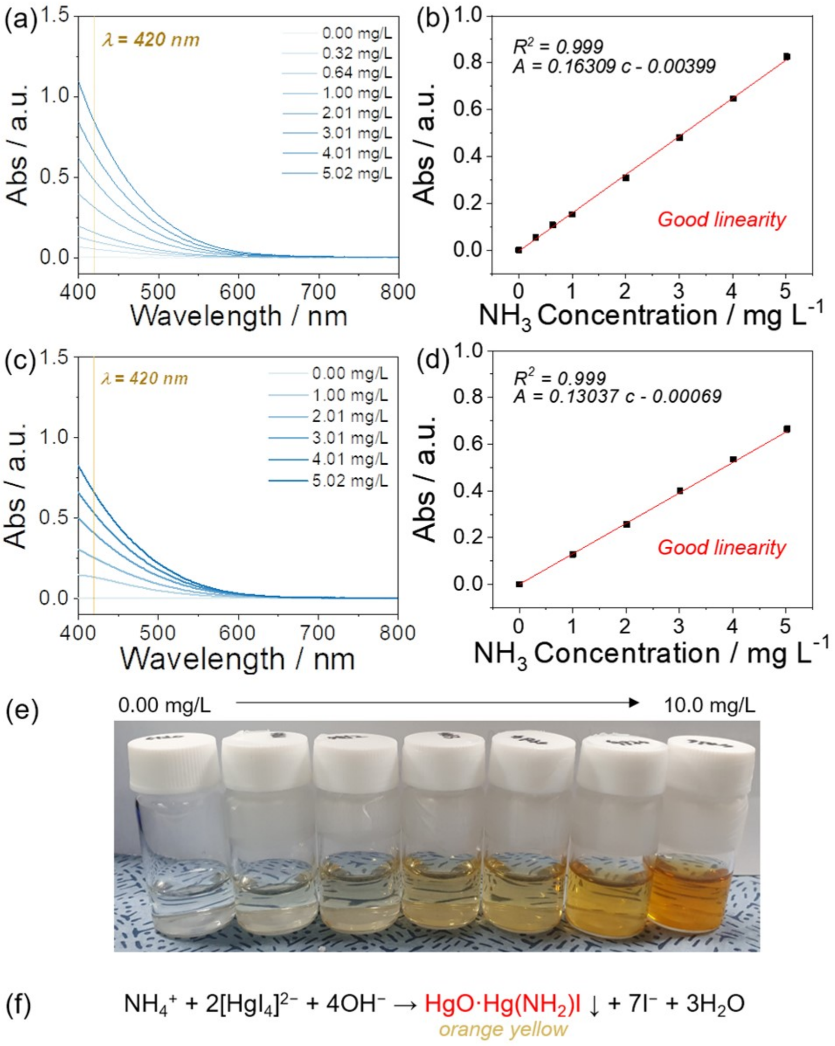

Figure S9. UV-Vis titration of Nessler's reagents for quantitative ammonia detection in alkaline and acidic conditions, applied for analytes in the working-electrode chamber and the acid-trap container, respectively. Representative absorptions and calibration curve for (a-b) 0.1 M KOH solution and (c, d) 5 mM H_2SO_4 solution. Each point is an average of 3 independent measurement results. (e) Digital photo of standard solutions with different concentrations of NH_3 and (f) chemical equation of ammonia detection using Nessler's reagent.

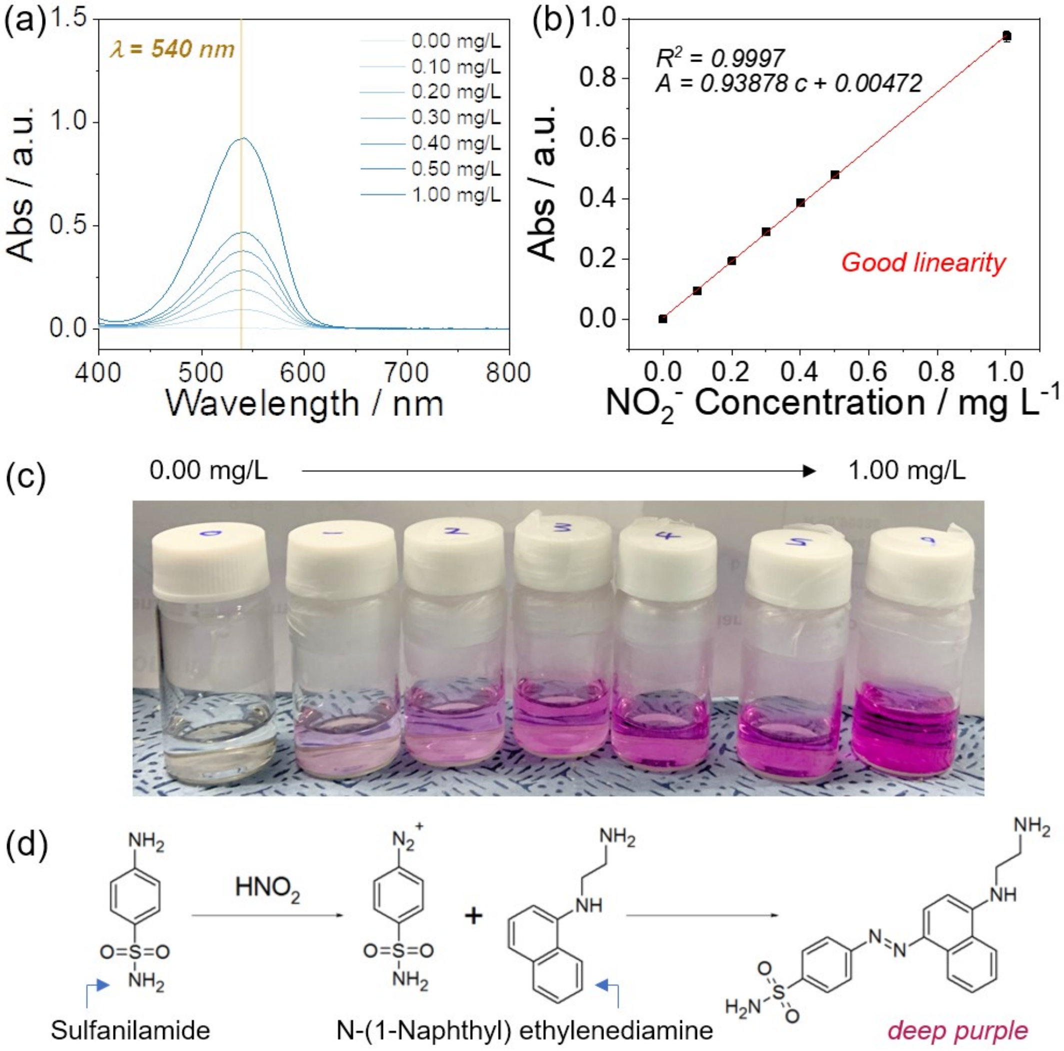

Figure S10. UV-Vis titration of Griess test for quantitative NO_2^- detection in alkaline and acidic conditions. (a) Representative absorption curves and (b) calibration curve of NO_2^- detection. Each point is an average of 3 independent measurement results. (c) Digital photo of standard solutions with different concentrations of NO_2^- and (d) chemical equation of Griess test.

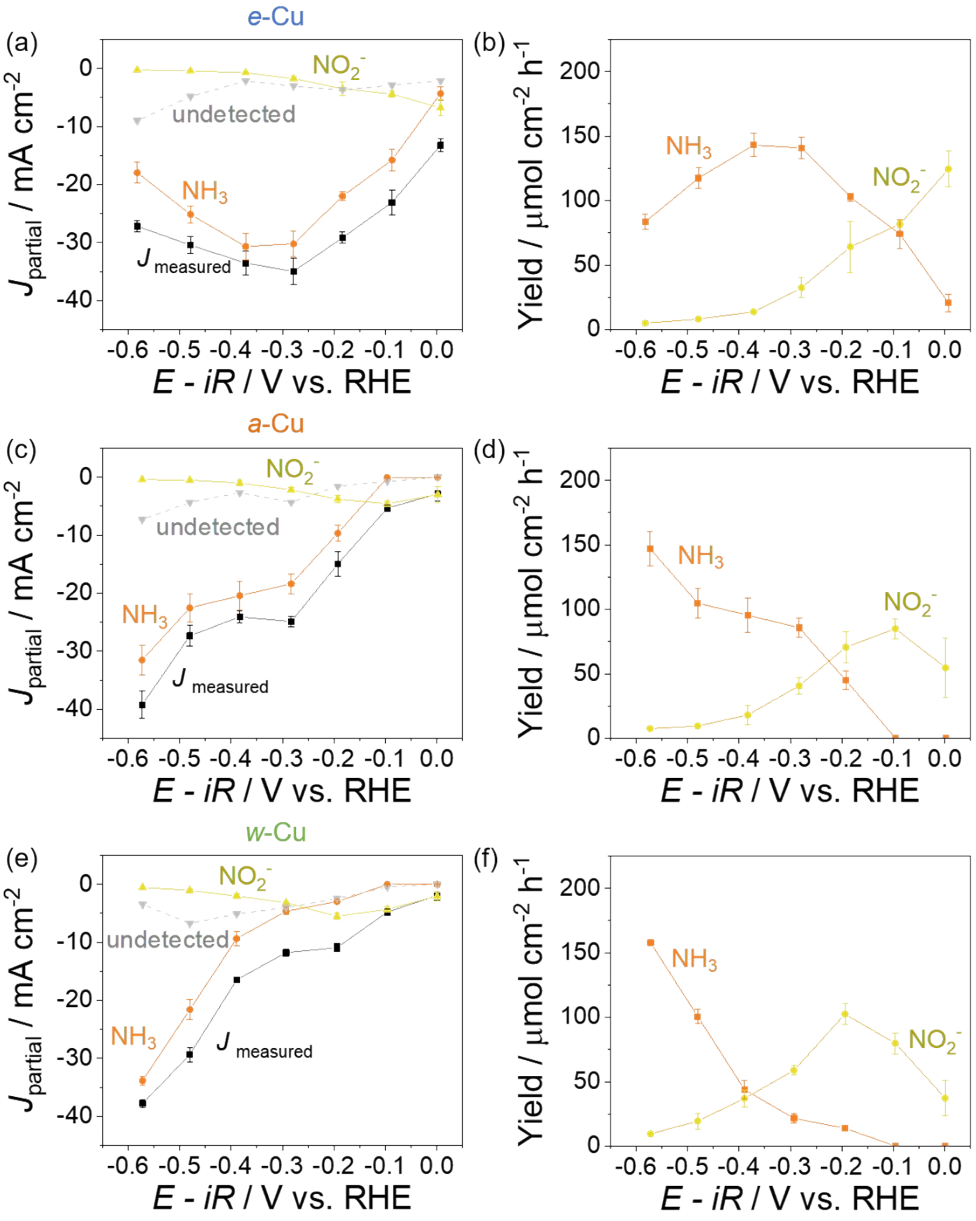

Figure S11. Potential-dependent NO_3RR efficiency for (a-b) *e*-Cu, (c-d) *a*-Cu, and (e-f) *w*-Cu electrodes. (a, c, e) Partial current density ($J_{partial}$) and (b, d, f) product yield after 1 h 50 mM NO_3^- reduction. The $J_{partial}$ for 'undetected' was estimated from the following equation.

$$J_{undetected}\,(mA\ cm^{-2}) = J_{averaged} - J_{NH_3} - J_{NO_2^-} \qquad \text{(Eq. S12)}$$

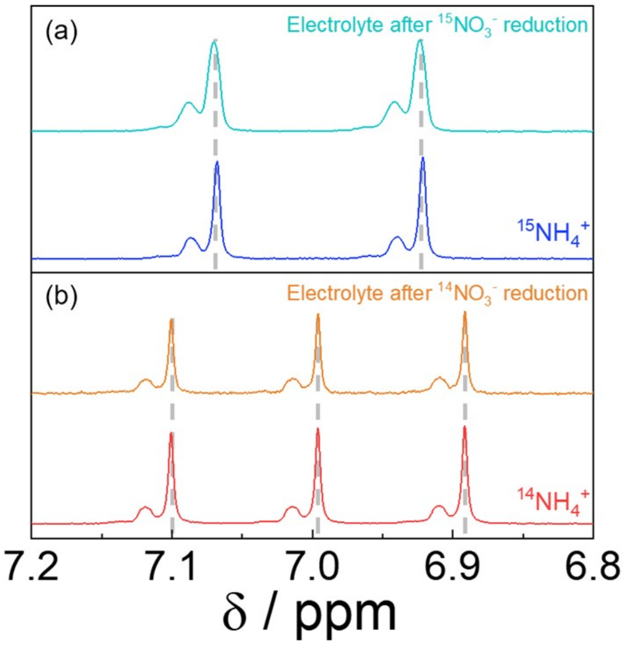

Figure S12. ^1H NMR spectra for isotopic analysis of (a) $^{15}NH_4^+$ and (b) $^{14}NH_4^+$. The bottom spectra are the standard solution of (a) $^{15}NH_4^+$ and (b) $^{14}NH_4^+$. The top spectra are the electrolyte solution after 1 h of (a) $^{15}NO_3^-$ and (b) $^{14}NO_3^-$ reduction on *e*-Cu at -0.4 V vs. RHE.

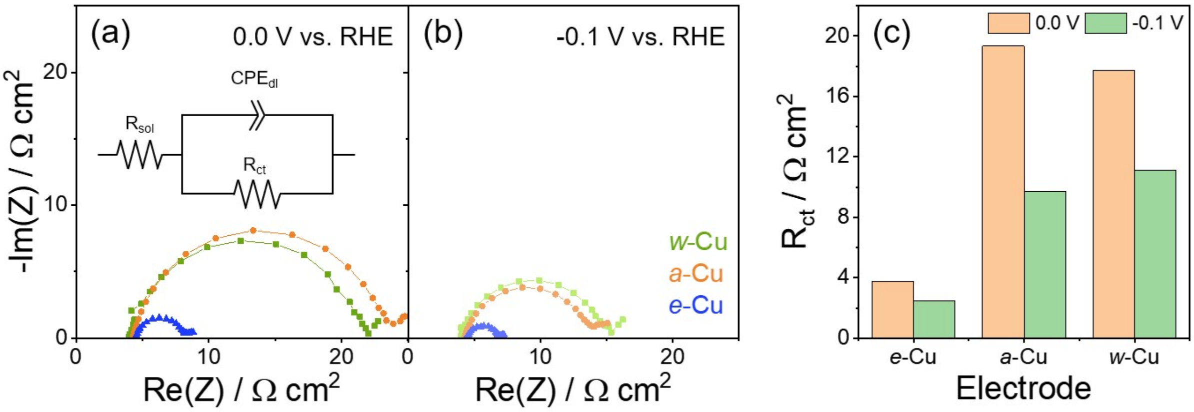

Figure S13. Electrochemical impedance spectroscopy (EIS) analysis of Cu electrodes. (a-b) Nyquist plots at (a) 0.0 V and (b) -0.1 V vs. RHE. The EIS was conducted in a 10^6 ~ 10^{-1} Hz frequency range with 10 mV voltage amplitude. The equivalent circuit model was included in the inset of (a), where R_{sol}, R_{ct}, and CPE_{dl} represent solution resistance, charge transfer resistance, and constant phase element for double-layer capacitance, respectively. (c) Estimated R_{ct} at 0.0 V and -0.1 V vs. RHE based on the equivalent circuit model. The estimated charge-transfer resistances are 3.78, 19.35, 17.71 Ω cm² at 0.0 V, and 2.45, 9.73, 11.14 Ω cm² at –0.1 V for *e*-Cu, *a*-Cu, and *w*-Cu, respectively.

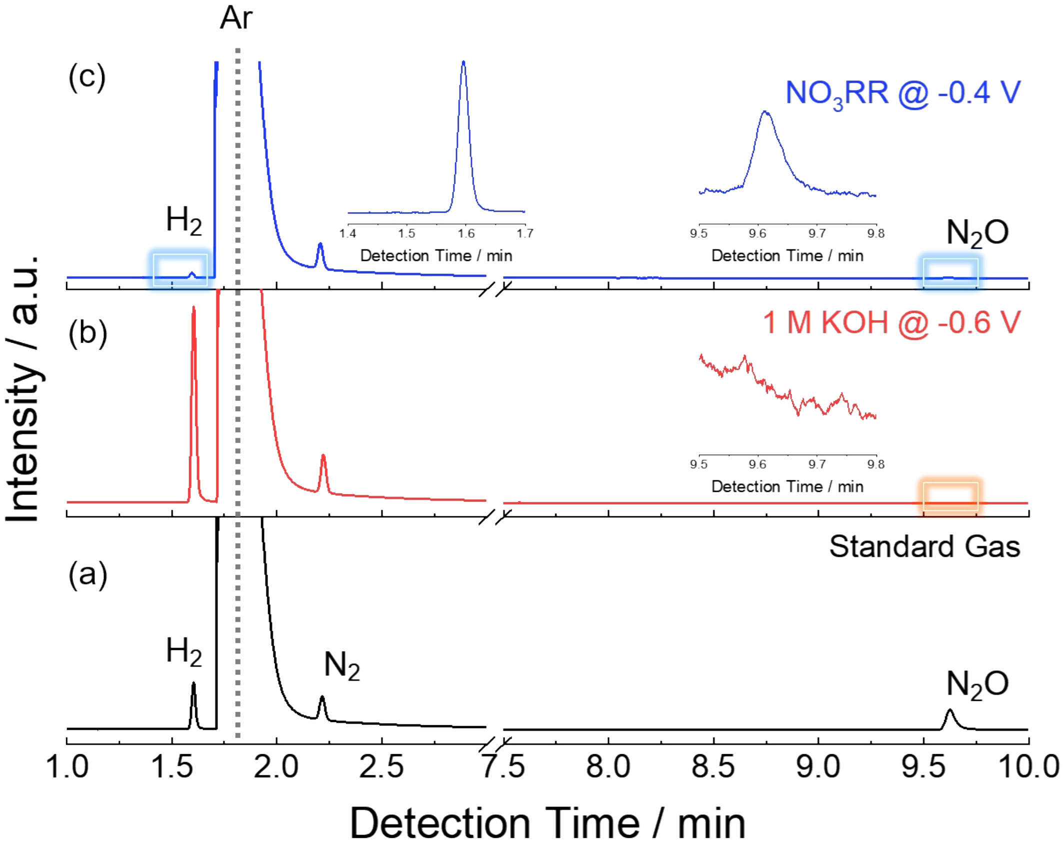

Figure S14. Qualitative analysis for undetected species from *w*-Cu. Gas-chromatograms of (a) standard gas with H_2 (1000 ppm), N_2 (200 ppm), and N_2O (200 ppm), balanced by Ar gas, (b) gas products from NO_3^- free 1 M KOH electrolyte solution after 15 min cathodic reaction at -0.6 V vs. RHE, and (c) gas products from 50 mM KNO_3 included 1 M KOH solution after 15 min NO_3RR at -0.4 V vs. RHE. The insets indicate high-magnified signals of H_2 (1.4 ~ 1.7 min) and N_2O (9.5 ~ 9.8 min). H_2, N_2, and N_2O gases were detected from *w*-Cu after NO_3RR, where we cannot rule out the presence of N_2 from air during the electrochemical cell assembly.

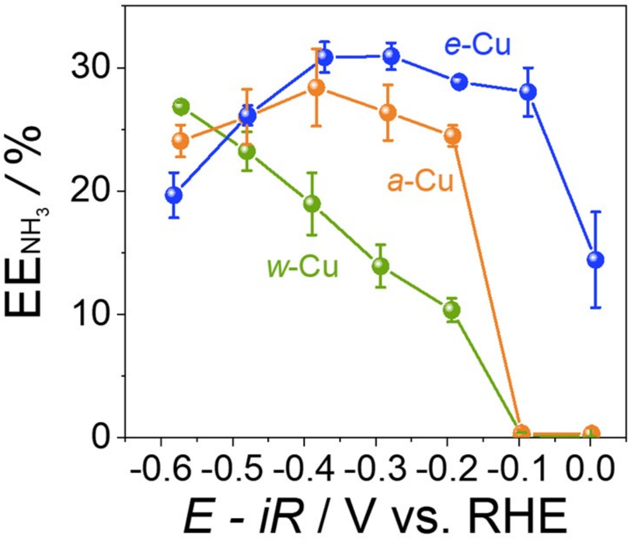

Figure S15. Potential-dependent half-cell energy efficiency (EE) for NH_3 electro-synthesis. Half-cell EE was calculated in the following equation,[34] where voltage efficiency (VE) for NH_3, Faradaic efficiency for NH_3 (FE_{NH3}), equilibrium potential of NO_3^- to NH_3 reduction ($E_{NH_3}^0$, 0.69 V_{RHE}), and applied potential after *iR* compensation (E) were included.

$$EE_{NH_3} = VE \times FE_{NH_3} = \frac{\left(1.23 - E_{NH_3}^0\right) FE_{NH_3}}{1.23 - E} \qquad \text{(Eq. S13)}$$

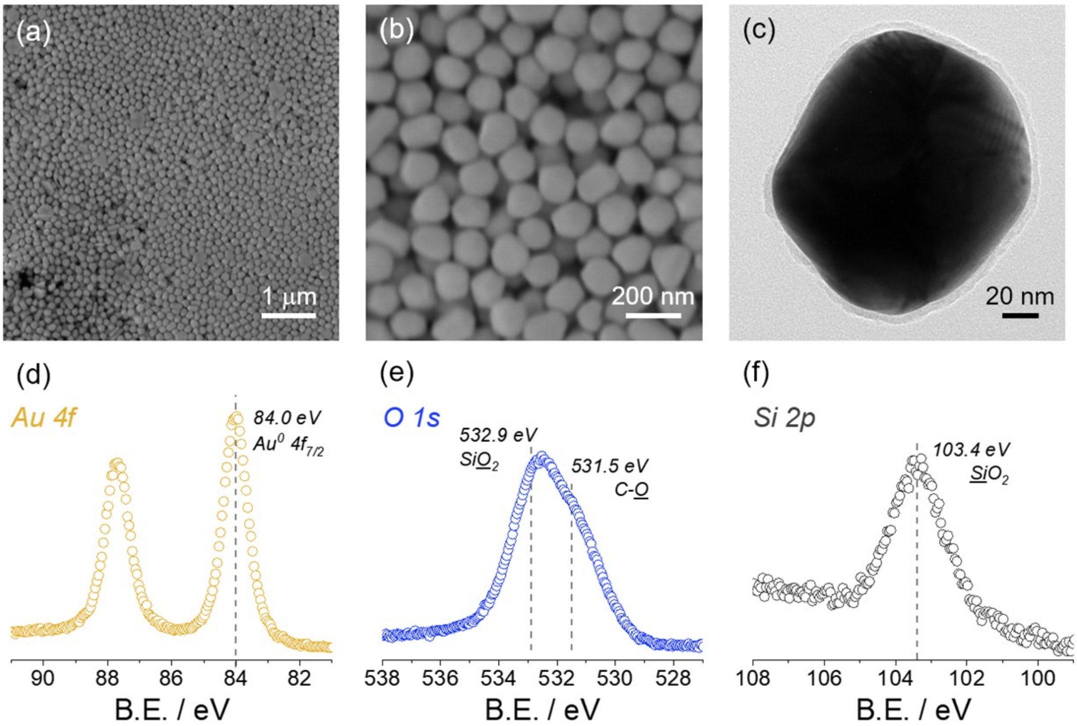

Figure S16. Characteristics of Au@SiO_2. (a-b) SEM images, (c) TEM image, and (d-f) XPS spectra in (d) Au 4f, (e) O 1s, and (f) Si 2p BE regions.[32] The Au diameter was ~150 nm, and the SiO_2 shell thickness was 4 ~ 6 nm. XPS spectra were calibrated by Au^0 $4f_{7/2}$ to 84.0 eV.

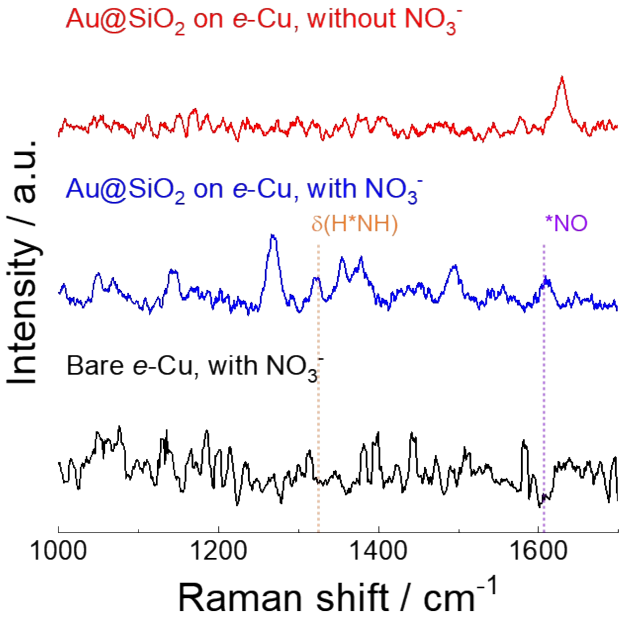

Figure S17. Effect of shell-isolated nanoparticles (SHIN) on SERS for the *e*-Cu surface at -0.1 V vs. RHE in 1 M KOH. A 50 mM KNO_3 was used in the case of the NO_3^- inclusion.

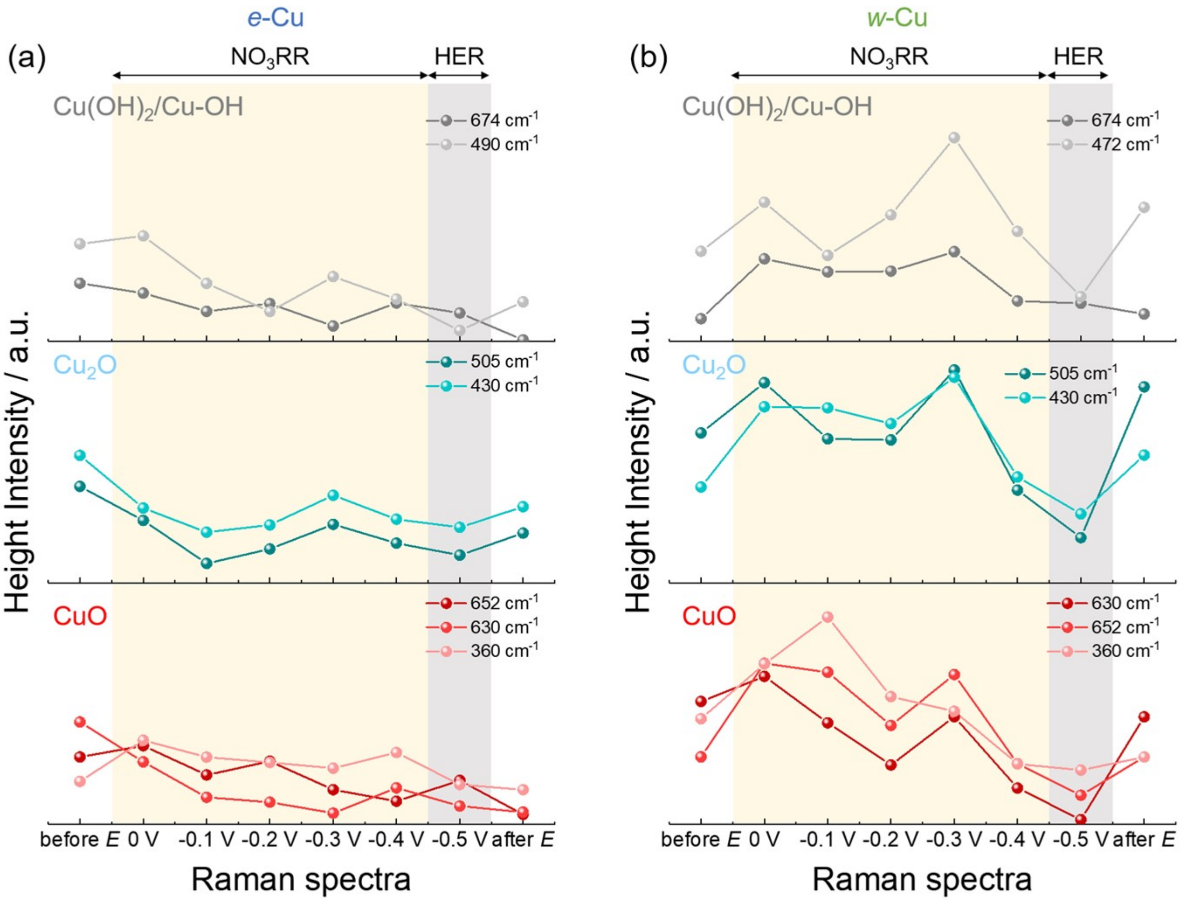

Figure S18. Potential-dependent Raman signal intensities for Cu(OH)$_2$/Cu-OH, Cu$_2$O, and CuO (from top to bottom panels) from (a) *e*-Cu and (b) *w*-Cu, with the same intensity scale.

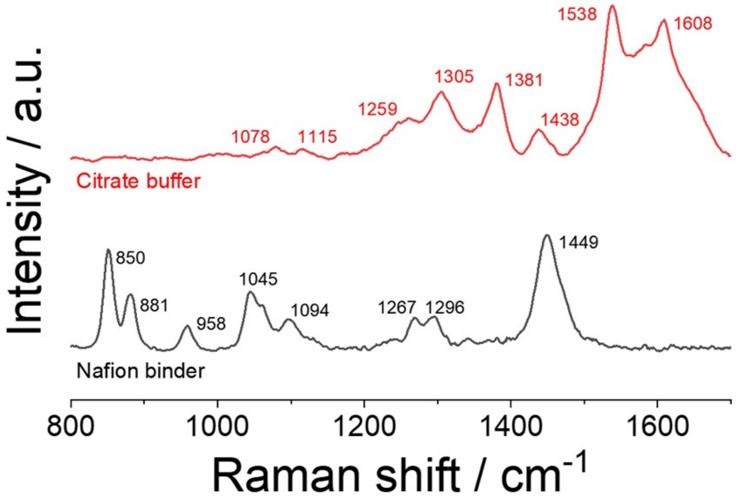

Figure S19. Raman spectra of citrate buffer and Nafion binder under the same measurement condition of Raman signal collecting of *operando* SHINERS.

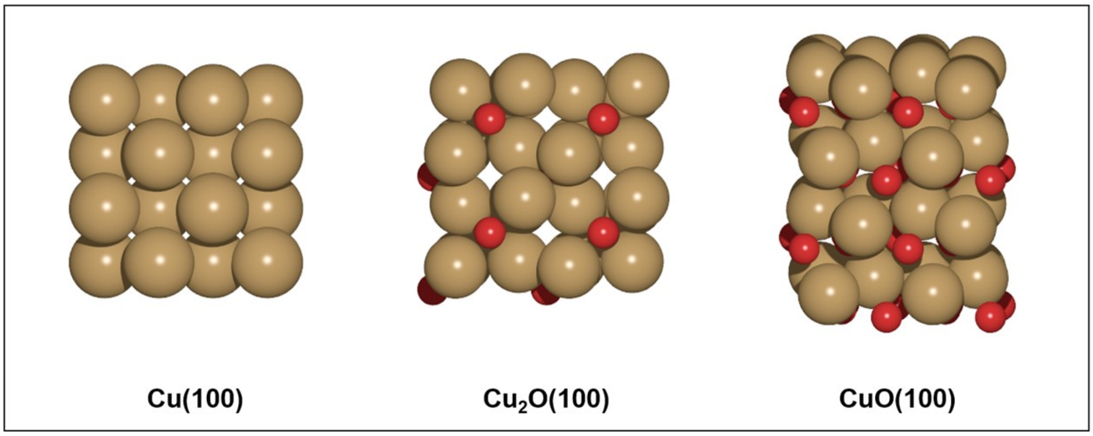

Figure S20. The structural model of Cu(100), $Cu_2O(100)$ and CuO(100).

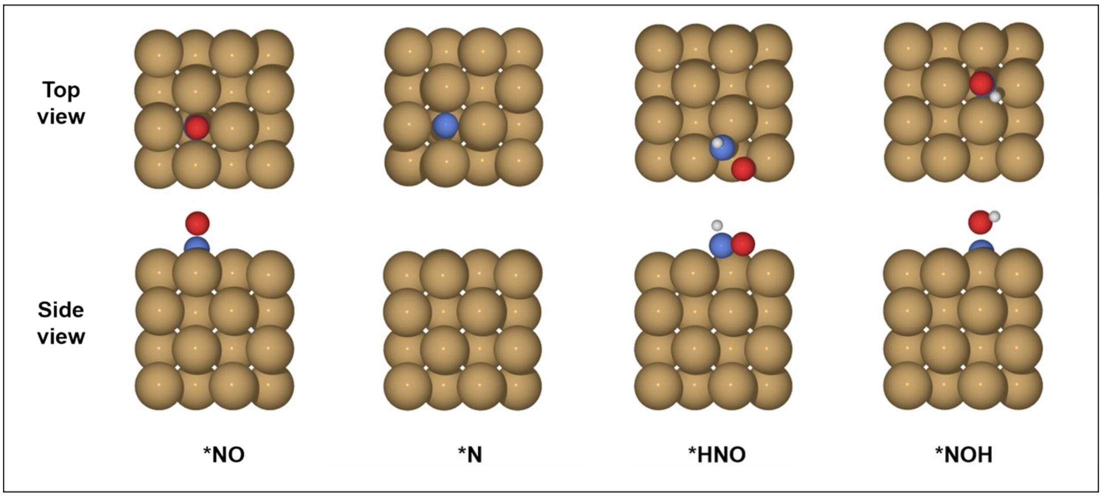

Figure S21. The optimized structures of four intermediates adsorbed on Cu(100).

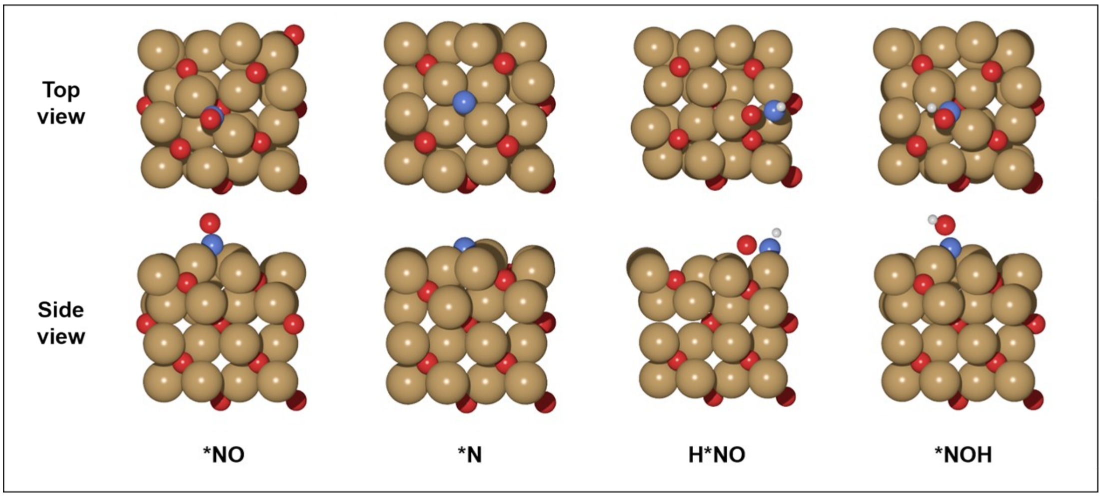

Figure S22. The optimized structures of four intermediates adsorbed on $Cu_2O(100)$.

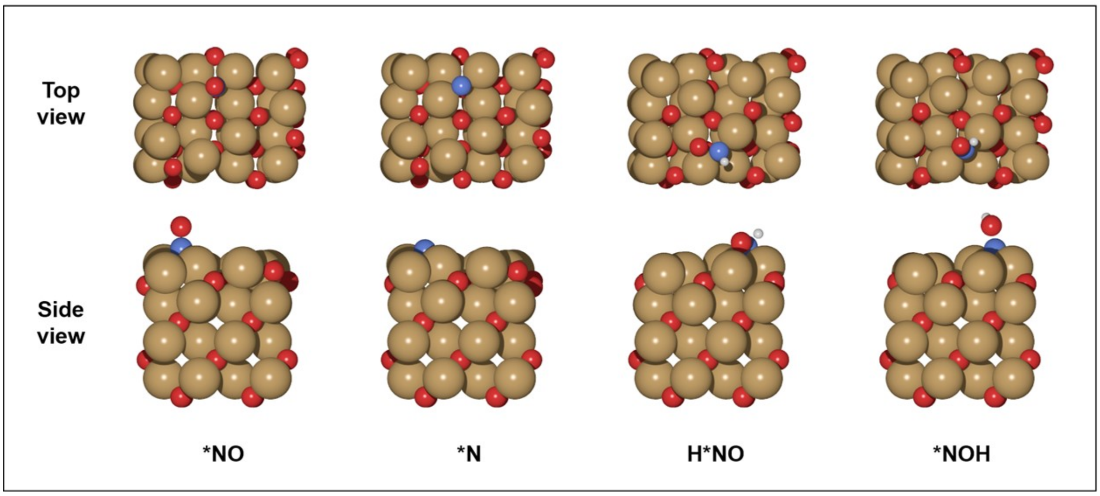

Figure S23. The optimized structures of four intermediates adsorbed on CuO(100).

Table S1. Comparative Tafel slope for Cu-based NO_3RR electrocatalysts.

Electrocatalyst	**Tafel slope ($mV\ dec^{-1}$)**	**[NO_3^-]**	**Electrolyte**	**Ref #**
e-Cu	71.4	50 mM	1 M KOH	This work
w-Cu	105.5			
a-Cu	129.0			
Cu_2O at Ni foam	90	50 mM	0.5 M Na_2SO_4	[35]
PO_4^{3-} modified Cu_2S nanowire	94	10 mM	0.1 M KOH	[36]
Cu foil	122	1 M	1 M KOH	[37]
Cu foil	130	20 mM	0.1 M $Na_xH_{3-x}PO_4$	[38]
Electrodeposited Cu	130	0.1 M	0.1 M H_2SO_4	[39]
Cu at Ni foam	130.6	200 ppm	1 M KOH	[40]
Polycrystalline Cu	206	1 mM	0.1 M $HClO_4$	[41]

Table S2. Surface area and roughness factor measurement by AFM. The roughness factor was converted from the RMS surface roughness using the Gwyddion program, assuming a projected area of 100 μm^2.

	As prepared Electrodes		
	Projected area (μm^2)	Surface area (μm^2)	Roughness factor [a]
e-Cu	100	100.3	1.003
a-Cu		101.8	1.018
w-Cu		100.9	1.009

[a.] calculated from the ratio between projected and measured surface area.

Table S3. Electrical double layer capacitance (EDLC), electrochemical surface area (ECSA), and roughness factor of Cu electrodes before and after 4 cycles of NO_3RR CV (**Figure S8**).

	Before NO_3RR CV			After 4 cycles of NO_3RR CV		
	EDLC [a] (μF cm^{-2}_{geo})	ECSA [b] (cm^2_{ECSA})	Roughness factor [c]	EDLC [a] (μF cm^{-2}_{geo})	ECSA [b] (cm^2_{ECSA})	Roughness factor [c]
e-Cu	72.2	1.81	1.1	233.1	5.83	3.6
a-Cu	136.7	3.42	1.8	189.8	4.75	2.5
w-Cu	168.4	4.21	2.6	178.6	4.47	2.7

[a.] 'geo' indicates geometrical surface area.

[b.] converted from EDLC with a specific capacitance of flat metal electrode (40 μF cm^{-2} $_{ECSA}$)[8, 42, 43]

[c.] calculated from the ratio between ECSA and geometrical surface area.

Table S4. Assigned Raman shifts for Cu oxides and hydroxides

Assignment	Raman shift / cm^{-1}		
	Measured	Reference	Ref #
CuO	360	332, 340, 347	2, 44, 45
	588	590	45
	630, 635	631	
	653	650	44
Cu_2O	430	412, 415	11, 45, 46
	506	502, 509	
	528	528	
	615	618, 619, 623	
$Cu(OH)_x$	463	460	45
	489	490	
	674	680	47

Table S5. Measured and calculated Raman shifts of NO_3RR intermediates

Assignment		**Raman shift / cm^{-1}**			
		Measured	Calculated	Reference	Ref #
NO_3^-	ν_s (NO_3^*)	1015, 1018	-	1015, 1018	11, 48
	ν_s (NO_3^-) stretch	1047, 1049	1032	1044	
	ν_{as} (NO_3^-) stretch	1345, 1352, 1366	1324	1350, 1372	
NO_2^-	ν_s (NO_2^-) of $^*ONO^*$	1180, 1185	1285	1180	11, 48
	*O-NO	1193, 1200	-	1200	
	ν_{as} (NO_2^-) of $^*ONO^*$	1275, 1291	1249	1280	
	*ON=O	1367, 1370, 1377	-	1372-1374	
	*ON*=O	1428, 1442, 1450	1402	1434	
NO	Cu_2-N*=O	1608, 1617	1342 (bridge) 1497 (3-fold)	1605-1631	49
	Cu_3-N*=O			1610	
HNO	ν(N=O) of H*NO	1522, 1527	1283	1528, 1531	11
	H*NO bend, stretch	1534	1326	1534	
NH	N-H	1520	749	1520, 1526	50, 51
$-NH_2$	$^-NH_2$	1160	1453	1152	51
	δ_s (HNH)	1308, 1311, 1320		1307	11
NH_3	NH_3	998	978	998	35
	δ_s (HNH)	1564, 1569, 1578	1599	1582, 1591	11

* indicating the surface adsorbed atom

Table S6. Gibbs free energy calculation corrected by pH for the four reactions.

Reaction	pH correction Gibbs free energy
$*NO_2 + 2H^+ + 2e^- \rightarrow *NO + H_2O$	$\Delta G_1 = \Delta G_R + 2k_BTln10 * pH$
$*NO + 2H^+ + 2e^- \rightarrow *N + H_2O$	$\Delta G_2 = \Delta G_R + 2k_BTln10 * pH$
$*NO + H^+ + e^- \rightarrow H*NO$	$\Delta G_3 = \Delta G_R + k_BTln10 * pH$
$*NO + H^+ + e^- \rightarrow *NOH$	$\Delta G_4 = \Delta G_R + k_BTln10 * pH$

Table S7. Calculated Gibbs free energy (in eV) on different catalysts at pH = 14.

	Cu(100)	Cu_2O(100)	CuO(100)
ΔG_1	0.750	0.765	0.842
ΔG_2	-0.027	1.874	1.969
ΔG_3	0.306	0.829	0.847
ΔG_4	0.665	1.026	1.690

Table S8. Energy, correction of zero-point energy, and enthalpic contribution of gas corrections for H_2O and H_2 used in the Gibbs free energy calculations.

Molecule	E (eV)	ZPE (eV) [a]	TΔS (eV) [b]
H_2O	-14.22	0.27	0.67
H_2	-6.76	0.57	0.41

[a] Data from T. Hu *et al.* [52]

[b] Data from J. K. R. Nørskov, J. *et al.* [28]

References

1. K. L. Chavez and D. W. Hess, *J. Electrochem. Soc.*, 2001, **148**, G640-G643.
2. K. Jiang, Y. Huang, G. Zeng, F. M. Toma, W. A. Goddard and A. T. Bell, *ACS Energy Lett.*, 2020, **5**, 1206-1214.
3. T. Kim and G. T. R. Palmore, *Nat. Commun.*, 2020, **11**, 3622.
4. D. Gao, I. Zegkinoglou, N. J. Divins, F. Scholten, I. Sinev, P. Grosse and B. Roldan Cuenya, *ACS Nano*, 2017, **11**, 4825-4831.
5. D. Gao, I. Sinev, F. Scholten, R. M. Aran-Ais, N. J. Divins, K. Kvashnina, J. Timoshenko and B. Roldan Cuenya, *Angew. Chem. Int. Ed. Engl.*, 2019, **58**, 17047-17053.
6. W. Jung and Y. J. Hwang, *Mater. Chem. Front.*, 2021, **5**, 6803-6823.
7. R. Jia, Y. Wang, C. Wang, Y. Ling, Y. Yu and B. Zhang, *ACS Catal.*, 2020, **10**, 3533-3540.
8. Y. Wang, W. Zhou, R. Jia, Y. Yu and B. Zhang, *Angew. Chem. Int. Ed. Engl.*, 2020, **59**, 5350-5354.
9. J. F. Li, X. D. Tian, S. B. Li, J. R. Anema, Z. L. Yang, Y. Ding, Y. F. Wu, Y. M. Zeng, Q. Z. Chen, B. Ren, Z. L. Wang and Z. Q. Tian, *Nat. Protoc.*, 2013, **8**, 52-65.
10. J. F. Li, Y. F. Huang, Y. Ding, Z. L. Yang, S. B. Li, X. S. Zhou, F. R. Fan, W. Zhang, Z. Y. Zhou, D. Y. Wu, B. Ren, Z. L. Wang and Z. Q. Tian, *Nature*, 2010, **464**, 392-395.
11. D. P. Butcher and A. A. Gewirth, *Nano Energy*, 2016, **29**, 457-465.
12. M. J. T. Frisch, G. W.; Schlegel, H. B.; Scuseria, G. E.; Robb, M. A.; Cheeseman, J. R.; Scalmani, G.; Barone, V.; Petersson, G. A.; Nakatsuji, H.; Li, X.; Caricato, M.; Marenich, A. V.; Bloino, J.; Janesko, B. G.; Gomperts, R.; Mennucci, B.; Hratchian, H. P.; Ortiz, J. V.; Izmaylov, A. F.; Sonnenberg, J. L.; Williams; Ding, F.; Lipparini, F.; Egidi, F.; Goings, J.; Peng, B.; Petrone, A.; Henderson, T.; Ranasinghe, D.; Zakrzewski, V. G.; Gao, J.; Rega, N.; Zheng, G.; Liang, W.; Hada, M.; Ehara, M.; Toyota, K.; Fukuda, R.; Hasegawa, J.; Ishida, M.; Nakajima, T.; Honda, Y.; Kitao, O.; Nakai, H.; Vreven, T.; Throssell, K.; Montgomery Jr., J. A.; Peralta, J. E.; Ogliaro, F.; Bearpark, M. J.; Heyd, J. J.; Brothers, E. N.; Kudin, K. N.; Staroverov, V. N.; Keith, T. A.; Kobayashi, R.; Normand, J.; Raghavachari, K.; Rendell, A. P.; Burant, J. C.; Iyengar, S. S.; Tomasi, J.; Cossi, M.; Millam, J. M.; Klene, M.; Adamo, C.; Cammi, R.; Ochterski, J. W.; Martin, R. L.; Morokuma, K.; Farkas, O.; Foresman, J. B.; Fox, D. J., *Journal*, 2010.
13. L.-B. Zhao, M. Zhang, Y.-F. Huang, C. T. Williams, D.-Y. Wu, B. Ren and Z.-Q. Tian, *J. Phys. Chem. Lett.*, 2014, **5**, 1259-1266.
14. P. J. Hay and W. R. Wadt, *J. Chem. Phys.*, 1985, **82**, 270-283.
15. G. Kresse and J. Furthmüller, *Phys. Rev. B*, 1996, **54**, 11169-11186.
16. V. I. Z. Anisimov, J.; Andersen, O. K., *Phys. Rev. B*, 1991, **44** 943–954.
17. A. I. A. Liechtenstein, V. I.; Zaanen, J., *Phys. Rev. B*, 1995, **52** R5467–R5470.
18. P. E. Blöchl, *Phys. Rev. B*, 1994, **50** 17953–17979.
19. J. P. B. Perdew, K.; Ernzerhof, M., *Phys. Rev. Lett.*, 1996, **77** 3865–3868.
20. C. E. A. Ekuma, V. I.; Moreno, J.; Jarrell, M, *Eur. Phys. J. B*, 2014, **87**, 23.
21. A. K. R. Mishra, A.; de Leeuw, N. H., *J. Phys. Chem. C*, 2016, **120**, 2198–2214.
22. Y.-Y. D. Song, B.; Wang, S.-W.; Wang, Z.-R.; Zhang, M.; Tian, P.; Wang, G.-C.; Zhao, Z., *ACS Omega*, 2020, **5**, 6260–6269.
23. S. Grimme, *J. Comput. Chem.*, 2006, **27**, 1787–1799.
24. H. J. P. Monkhorst, J. D., *Phys. Rev. B* 1976, **13**, 5188–5192.
25. K. S. Mathew, R.; Letchworth-Weaver, K.; Arias, T. A.; Hennig, R. G. , *J. Chem. Phys.* , 2014, **140**, 084106.
26. L. T. Chen, C.; Davey, K.; Zheng, Y.; Jiao, Y.; Qiao, S.-Z., *Chem. Sci.*, 2021, **12**, 8079–8087.
27. G. U. Henkelman, B. P.; Jónsson, H. , *J. Chem. Phys.* , 2000, **113**, 9901–9904. .
28. J. K. R. Nørskov, J.; Logadottir, A.; Lindqvist, L.; Kitchin, J. R.; Bligaard, T.; Jónsson, H. , *J. Phys. Chem. B*, 2004, **108**, 17886–17892.

29. T. Jang, J.-H. Kang, S. Kim, M. Shim, J. Lee, J. Song, W. Kim, K. Ryu and H. R. Byon, *ACS Appl. Energy Mater.*, 2021, **4**, 2644-2651.
30. Y. Oh, J. Park, Y. Kim, M. Shim, T.-S. Kim, J. Y. Park and H. R. Byon, *J. Mater. Chem. A.*, 2021, **9**, 11210-11218.
31. D.-H. Nam, B. J. Taitt and K.-S. Choi, *ACS Catal.*, 2018, **8**, 1197-1206.
32. A. V., Naumkin, Anna Kraut-Vass, Stephen W. Gaarenstroom and C. J. Powell, *Journal*, 2000, DOI: doi:10.18434/T4T88K.
33. J. Choi, H.-L. Du, C. K. Nguyen, B. H. R. Suryanto, A. N. Simonov and D. R. MacFarlane, *ACS Energy Lett.*, 2020, DOI: 10.1021/acsenergylett.0c00924, 2095-2097.
34. Y. Wang, A. Xu, Z. Wang, L. Huang, J. Li, F. Li, J. Wicks, M. Luo, D. H. Nam, C. S. Tan, Y. Ding, J. Wu, Y. Lum, C. T. Dinh, D. Sinton, G. Zheng and E. H. Sargent, *J. Am. Chem. Soc.*, 2020, **142**, 5702-5708.
35. C. Wang, F. Ye, J. Shen, K.-H. Xue, Y. Zhu and C. Li, *ACS Appl. Mater. Interfaces*, 2022, **14**, 6680-6688.
36. W. He, J. Zhang, S. Dieckhofer, S. Varhade, A. C. Brix, A. Lielpetere, S. Seisel, J. R. C. Junqueira and W. Schuhmann, *Nat. Commun.*, 2022, **13**, 1129.
37. W. Lin, E. Zhou, J. F. Xie, J. Lin and Y. Wang, *Adv. Funct. Mater.*, 2022, **32**, 2209464.
38. O. Q. Carvalho, S. R. S. Jones, A. E. Berninghaus, R. F. Hilliard, T. S. Radniecki and K. A. Stoerzinger, *Electrochem. Sci. Adv.*, 2022, DOI: 10.1002/elsa.202100201.
39. G. E. Dima, A. C. A. de Vooys and M. T. M. Koper, *J. Electroanal. Chem.*, 2003, **554-555**, 15-23.
40. J. Li, J. Gao, T. Feng, H. Zhang, D. Liu, C. Zhang, S. Huang, C. Wang, F. Du, C. Li and C. Guo, *J. Power Sources*, 2021, **511**.
41. S.-E. Bae, K. L. Stewart and A. A. Gewirth, *J. Am. Chem. Soc.* , 2007, **129**, 10171-10180.
42. Y. Wang, H. Li, W. Zhou, X. Zhang, B. Zhang and Y. Yu, *Angew. Chem. Int. Ed. Engl.*, 2022, **61**, e202202604.
43. C. C. McCrory, S. Jung, J. C. Peters and T. F. Jaramillo, *J. Am. Chem. Soc.*, 2013, **135**, 16977-16987.
44. T. H. M. Pham, J. Zhang, M. Li, T. H. Shen, Y. Ko, V. Tileli, W. Luo and A. Züttel, *Adv. Energy Mater.*, 2022, **12**, 2103663.
45. Y. Deng, A. D. Handoko, Y. Du, S. Xi and B. S. Yeo, *ACS Catal.*, 2016, **6**, 2473-2481.
46. M. He, X. Chang, T.-H. Chao, C. Li, W. A. Goddard, M.-J. Cheng, B. Xu and Q. Lu, *ACS Catal.*, 2022, DOI: 10.1021/acscatal.2c00087, 6036-6046.
47. N. Bodappa, M. Su, Y. Zhao, J. B. Le, W. M. Yang, P. Radjenovic, J. C. Dong, J. Cheng, Z. Q. Tian and J. F. Li, *J. Am. Chem. Soc.*, 2019, **141**, 12192-12196.
48. L. H. Zhang, Y. Jia, J. Zhan, G. Liu, G. Liu, F. Li and F. Yu, *Angew. Chem. Int. Ed. Engl.*, 2023, **62**, e202303483.
49. W. A. Brown and D. A. King, *J. Phys. Chem. B* 2000, **104**, 2578-2595.
50. S. Liu, T. Qian, M. Wang, H. Ji, X. Shen, C. Wang and C. Yan, *Nat. Catal.*, 2021, **4**, 322–331.
51. M. Wang, S. Liu, H. Ji, T. Yang, T. Qian and C. Yan, *Nat. Commun.*, 2021, **12**.
52. T. Hu, C. Wang, M. Wang, C. M. Li and C. Guo, *ACS Catal.*, 2021, **11**, 14417-14427.